Towards Understanding the Origin of Cosmic-Ray Electrons

M. Aguilar,[26] L. Ali Cavasonza,[1] B. Alpat,[31] G. Ambrosi,[31] L. Arruda,[24] N. Attig,[21] P. Azzarello,[15] A. Bachlechner,[1] F. Barao,[24] A. Barrau,[16] L. Barrin,[14] A. Bartoloni,[36] L. Basara,[34] S. Başeğmez-du Pree,[17] R. Battiston,[34,35,*] U. Becker,[10] M. Behlmann,[10] B. Beischer,[1] J. Berdugo,[26] B. Bertucci,[31,32] V. Bindi,[19] W. de Boer,[22] K. Bollweg,[20] B. Borgia,[36,37] M. J. Boschini,[28] M. Bourquin,[15] E. F. Bueno,[38] J. Burger,[10] W. J. Burger,[34] X. D. Cai,[10] M. Capell,[10] S. Caroff,[3] J. Casaus,[26] G. Castellini,[13] F. Cervelli,[33] Y. H. Chang,[43] G. M. Chen,[6] H. S. Chen,[6,7] Y. Chen,[15] L. Cheng,[39] H. Y. Chou,[43] V. Choutko,[10] C. H. Chung,[1] C. Clark,[10,20] G. Coignet,[3] C. Consolandi,[19] A. Contin,[8,9] C. Corti,[19] M. Crispoltoni,[31,32] Z. Cui,[39] K. Dadzie,[10] Y. M. Dai,[5] A. Datta,[19] C. Delgado,[26] S. Della Torre,[28] M. B. Demirköz,[2] L. Derome,[16] S. Di Falco,[33] V. Di Felice,[31,†] F. Dimiccoli,[14,34] C. Díaz,[26] P. von Doetinchem,[19] F. Dong,[30] F. Donnini,[31,†] M. Duranti,[31] A. Egorov,[10] A. Eline,[10] T. Eronen,[44] J. Feng,[10] E. Fiandrini,[31,32] P. Fisher,[10] V. Formato,[31] Y. Galaktionov,[10] R. J. García-López,[23] C. Gargiulo,[14] H. Gast,[1] I. Gebauer,[22] M. Gervasi,[28,29] F. Giovacchini,[26] D. M. Gómez-Coral,[27] J. Gong,[30] C. Goy,[3] V. Grabski,[27] D. Grandi,[28,29] M. Graziani,[22] K. H. Guo,[18] S. Haino,[42] K. C. Han,[25] Z. H. He,[18] M. Heil,[10] T. H. Hsieh,[10] H. Huang,[42,‡] Z. C. Huang,[18] M. Incagli,[33] Yi Jia,[10] H. Jinchi,[25] K. Kanishev,[34] B. Khiali,[31,†] Th. Kirn,[1] C. Konak,[2] O. Kounina,[10] A. Kounine,[10] V. Koutsenko,[10] A. Kulemzin,[10] G. La Vacca,[28,29] E. Laudi,[14] G. Laurenti,[8] I. Lazzizzera,[34,35] A. Lebedev,[10] H. T. Lee,[41] S. C. Lee,[42] C. Leluc,[15] J. Q. Li,[30] Q. Li,[30] T. X. Li,[18] Z. H. Li,[6] C. Light,[19] C. H. Lin,[42] T. Lippert,[21] F. Z. Liu,[10] Hu Liu,[10,43] Z. Liu,[15] S. Q. Lu,[18] Y. S. Lu,[6] K. Luebelsmeyer,[1] F. Luo,[39] J. Z. Luo,[30] Xi Luo,[19] S. S. Lyu,[18] F. Machate,[1] C. Mañá,[26] J. Marín,[26] T. Martin,[10,20] G. Martínez,[26] N. Masi,[8] D. Maurin,[16] A. Menchaca-Rocha,[27] Q. Meng,[30] D. C. Mo,[18] M. Molero,[26] P. Mott,[10,20] L. Mussolin,[31,32] T. Nelson,[19] J. Q. Ni,[18] N. Nikonov,[1] F. Nozzoli,[34] A. Oliva,[26] M. Orcinha,[24] M. Palermo,[19] F. Palmonari,[8,9] M. Paniccia,[15] A. Pashnin,[10] M. Pauluzzi,[31,32] S. Pensotti,[28,29] C. Perrina,[15] H. D. Phan,[10] N. Picot-Clemente,[12] V. Plyaskin,[10] M. Pohl,[15] V. Poireau,[3] A. Popkow,[19] L. Quadrani,[8,9] X. M. Qi,[18] X. Qin,[10] Z. Y. Qu,[42] P. G. Rancoita,[28] D. Rapin,[15] A. Reina Conde,[23] S. Rosier-Lees,[3] A. Rozhkov,[10] D. Rozza,[28,29] R. Sagdeev,[11] C. Solano,[10] S. Schael,[1] S. M. Schmidt,[21] A. Schulz von Dratzig,[1] G. Schwering,[1] E. S. Seo,[12] B. S. Shan,[4] J. Y. Shi,[30] T. Siedenburg,[1] J. W. Song,[39] Z. T. Sun,[6,7] M. Tacconi,[28,29] X. W. Tang,[6] Z. C. Tang,[6] J. Tian,[31,32] Samuel C. C. Ting,[10,14] S. M. Ting,[10] N. Tomassetti,[31,32] J. Torsti,[44] T. Urban,[10,20] V. Vagelli,[31,32] E. Valente,[36,37] E. Valtonen,[44] M. Vázquez Acosta,[23] M. Vecchi,[17,38] M. Velasco,[26] J. P. Vialle,[3] J. Vizán,[26] L. Q. Wang,[39] N. H. Wang,[39] Q. L. Wang,[5] X. Wang,[10] X. Q. Wang,[6,7] Z. X. Wang,[18] J. Wei,[15] Z. L. Weng,[10] H. Wu,[30] R. Q. Xiong,[30] W. Xu,[10] Q. Yan,[10] Y. Yang,[40] H. Yi,[30] Y. J. Yu,[5] Z. Q. Yu,[6] M. Zannoni,[28,29] S. Zeissler,[22] C. Zhang,[6] F. Zhang,[6] J. H. Zhang,[30] Z. Zhang,[10] F. Zhao,[6,7] Z. M. Zheng,[4] H. L. Zhuang,[6] V. Zhukov,[1] A. Zichichi,[8,9] N. Zimmermann,[1] and P. Zuccon[34,35]

(AMS Collaboration)

[1]*I. Physics Institute and JARA-FAME, RWTH Aachen University, D–52056 Aachen, Germany*
[2]*Department of Physics, Middle East Technical University (METU), 06800 Ankara, Turkey*
[3]*Univ. Grenoble Alpes, Univ. Savoie Mont Blanc, CNRS, LAPP-IN2P3, F–74000 Annecy, France*
[4]*Beihang University (BUAA), Beijing 100191, China*
[5]*Institute of Electrical Engineering (IEE), Chinese Academy of Sciences, Beijing 100190, China*
[6]*Institute of High Energy Physics (IHEP), Chinese Academy of Sciences, Beijing 100049, China*
[7]*University of Chinese Academy of Sciences (UCAS), Beijing 100049, China*
[8]*INFN Sezione di Bologna, I–40126 Bologna, Italy*
[9]*Università di Bologna, I–40126 Bologna, Italy*
[10]*Massachusetts Institute of Technology (MIT), Cambridge, Massachusetts 02139, USA*
[11]*East–West Center for Space Science, University of Maryland, College Park, Maryland 20742, USA*
[12]*IPST, University of Maryland, College Park, Maryland 20742, USA*
[13]*CNR–IROE, I–50125 Firenze, Italy*
[14]*European Organization for Nuclear Research (CERN), CH–1211 Geneva 23, Switzerland*
[15]*DPNC, Université de Genève, CH–1211 Genève 4, Switzerland*
[16]*Univ. Grenoble Alpes, CNRS, Grenoble INP, LPSC-IN2P3, F–38000 Grenoble, France*
[17]*KVI—Center for Advanced Radiation Technology, University of Groningen, NL–9700 AB Groningen, Netherlands*
[18]*Sun Yat–Sen University (SYSU), Guangzhou, 510275, China*
[19]*Physics and Astronomy Department, University of Hawaii, Honolulu, Hawaii 96822, USA*
[20]*National Aeronautics and Space Administration Johnson Space Center (JSC), Houston, Texas 77058, USA*

[21]Jülich Supercomputing Centre and JARA-FAME, Research Centre Jülich, D–52425 Jülich, Germany
[22]Institut für Experimentelle Teilchenphysik, Karlsruhe Institute of Technology (KIT), D–76131 Karlsruhe, Germany
[23]Instituto de Astrofísica de Canarias (IAC), E–38205 La Laguna, and Departamento de Astrofísica, Universidad de La Laguna, E–38206 La Laguna, Tenerife, Spain
[24]Laboratório de Instrumentação e Física Experimental de Partículas (LIP), P–1000 Lisboa, Portugal
[25]National Chung–Shan Institute of Science and Technology (NCSIST), Longtan, Tao Yuan, 32546, Taiwan
[26]Centro de Investigaciones Energéticas, Medioambientales y Tecnológicas (CIEMAT), E–28040 Madrid, Spain
[27]Instituto de Física, Universidad Nacional Autónoma de México (UNAM), México, D. F., 01000 Mexico
[28]INFN Sezione di Milano–Bicocca, I–20126 Milano, Italy
[29]Università di Milano–Bicocca, I–20126 Milano, Italy
[30]Southeast University (SEU), Nanjing, 210096, China
[31]INFN Sezione di Perugia, I–06100 Perugia, Italy
[32]Università di Perugia, I–06100 Perugia, Italy
[33]INFN Sezione di Pisa, I–56100 Pisa, Italy
[34]INFN TIFPA, I–38123 Povo, Trento, Italy
[35]Università di Trento, I–38123 Povo, Trento, Italy
[36]INFN Sezione di Roma 1, I–00185 Roma, Italy
[37]Università di Roma La Sapienza, I–00185 Roma, Italy
[38]Instituto de Física de São Carlos, Universidade de São Paulo, CP 369, 13560-970, São Carlos, São Paulo, SP, Brazil
[39]Shandong University (SDU), Jinan, Shandong, 250100, China
[40]National Cheng Kung University, Tainan, 70101, Taiwan
[41]Academia Sinica Grid Center (ASGC), Nankang, Taipei, 11529, Taiwan
[42]Institute of Physics, Academia Sinica, Nankang, Taipei, 11529, Taiwan
[43]Physics Department and Center for High Energy and High Field, National Central University (NCU), Tao Yuan, 32054, Taiwan
[44]Space Research Laboratory, Department of Physics and Astronomy, University of Turku, FI–20014 Turku, Finland

(Received 7 January 2019; published 13 March 2019)

Precision results on cosmic-ray electrons are presented in the energy range from 0.5 GeV to 1.4 TeV based on 28.1×10^6 electrons collected by the Alpha Magnetic Spectrometer on the International Space Station. In the entire energy range the electron and positron spectra have distinctly different magnitudes and energy dependences. The electron flux exhibits a significant excess starting from $42.1^{+5.4}_{-5.2}$ GeV compared to the lower energy trends, but the nature of this excess is different from the positron flux excess above 25.2 ± 1.8 GeV. Contrary to the positron flux, which has an exponential energy cutoff of 810^{+310}_{-180} GeV, at the 5σ level the electron flux does not have an energy cutoff below 1.9 TeV. In the entire energy range the electron flux is well described by the sum of two power law components. The different behavior of the cosmic-ray electrons and positrons measured by the Alpha Magnetic Spectrometer is clear evidence that most high energy electrons originate from different sources than high energy positrons.

DOI: 10.1103/PhysRevLett.122.101101

The precision measurement of the electron flux in primary cosmic rays with the Alpha Magnetic Spectrometer (AMS) on the International Space Station (ISS) is presented with a particular emphasis on the behavior at high energies. The measurement is based on 28.1×10^6 electron events collected by AMS from May 19, 2011 to November 12, 2017. This corresponds to a factor of 3 increase in statistics and a factor of 2 increase in the energy range compared to our results published nearly five years ago [1]. Complementary to the present data, we have also published the analysis of low energy complex time structures in cosmic-ray electron and positron fluxes during the same period [2]. AMS also performed detailed studies of positrons up to 1 TeV [3,4]. The observed new source of high energy positrons poses the question of the existence of a similar source in cosmic-ray electrons. In the past four years, there were many models explaining the AMS results on cosmic-ray electrons and positrons. They fall into three distinct classes: acceleration to high energies in astrophysical objects [5], production in the interactions of cosmic-ray nuclei with interstellar gas [6], and annihilation of dark matter particles [7]. Most of these explanations differ in their predictions for the behavior of cosmic-ray electrons and positrons at high energies. Several models based on our data [1] have been constructed to test the assumption of an identical source term for electrons and positrons [8,9]. Another model with a unique source term for electrons

from a supernova remnant has been proposed [10]. The comprehensive paper on results for all elementary particles from the first 6.5 years of AMS operations, which includes details of the analysis, particularly at high energies, and comparison with theoretical models, will be presented in a separate publication [11]. In this Letter we present precision measurements of primary cosmic-ray electrons up to 1.4 TeV and the comparison with our latest data on cosmic-ray positrons [4]. These results are crucial for providing insights into origins of high energy cosmic-ray electrons and positrons.

Detector.—The description of the AMS detector is presented in Ref. [12]. The key detector elements used for the present analysis are the transition radiation detector (TRD) [13], the time of flight counters (TOF) [14], the silicon tracker [15], the permanent magnet [16], and the electromagnetic calorimeter (ECAL) [17]. AMS also has an array of 16 anticoincidence counters [18] and a ring imaging Čerenkov detector [19]. The detector performance on orbit is continuously monitored and the overall AMS instrument response stability is $0.0 \pm 0.4\%$ [2,11].

The nine-layer tracker, $L1$–$L9$, accurately measures the rigidity R and the charge Z of cosmic rays. The maximum detectable rigidity is 2 TV. The TOF measures $|Z|$ and velocity β. The TRD separates electrons and positrons $e^{\pm}$ from protons p using a Λ_{TRD} estimator [3]. The ECAL accurately measures the $e^{\pm}$ energies and differentiates $e^{\pm}$ from p by exploiting their different shower shapes with a Λ_{ECAL} estimator [20] (see Supplemental Material [21] for a detailed description of the detector performance). A Monte Carlo program, based on the GEANT4 10.1 package [22], is used to simulate physics processes and signals in the detector. Examples of thorough understanding of the detector performance, particularly at high energies, are presented in Figs. S1–S4 of the Supplemental Material [21].

Event selection.—AMS has collected 1.07×10^{11} cosmic rays in the first 6.5 years of operation. The collection time used in this analysis includes only those seconds during which the detector was in normal operating conditions, AMS was pointing within 40° of the local zenith, and the ISS was outside of the South Atlantic Anomaly. Because of the influence of the geomagnetic field, this collection time for galactic cosmic rays increases with rigidity reaching 1.51×10^{8} s above 30 GeV.

Selected events are required to be downward going with $\beta > 0.8$, to have a shower in the ECAL with a geometrically matched track in the tracker and the TRD. For the analysis of the energy range $E \geq 290$ GeV, the track is required to pass through either $L1$ or $L9$. Track fitting quality criteria such as $\chi^2/\mathrm{d.o.f.} < 20$ both in the bending and nonbending planes are applied to ensure good accuracy of the track reconstruction. The charge measurements in TOF and tracker are required to be consistent with $|Z| = 1$.

The energy E is required to be greater than 1.2 times the maximum Størmer cutoff [23] within the AMS field of view. An alternative procedure, with the cutoff calculated by backtracing particles from the top of AMS out to 50 Earth's radii [24] using the most recent International Geomagnetic Reference Field [25], yields the same results.

Events satisfying the selection criteria are classified into two categories: positive and negative rigidity data samples. In this Letter we consider only the negative rigidity sample, which comprises mostly electrons and a small amount of charge confusion positrons and protons, that is, positrons and protons reconstructed in the tracker with negative rigidity due to the finite tracker resolution or due to interactions with the detector materials. The ECAL estimator Λ_{ECAL}, the TRD estimator Λ_{TRD}, and the charge confusion estimator $\Lambda^{e}_{\mathrm{CC}}$ [4,26] allow differentiation between the electron signal and the background from antiprotons and charge confusion protons. To distinguish electrons from charge confusion positrons, the charge confusion estimator $\Lambda^{e}_{\mathrm{CC}}$ is used.

In the energy range [0.5–1000] GeV an energy-dependent cut on the ECAL estimator Λ_{ECAL} is applied to remove most of the background from antiprotons and charge confusion protons. After this cut, the antiproton background is negligible; it constitutes less than 10^{-3} of the negative rigidity sample. Then, the number of electrons and its statistical error in each bin are determined by fitting signal and background templates to data by varying their respective normalizations. The two-dimensional $(\Lambda_{\mathrm{TRD}} - \Lambda^{e}_{\mathrm{CC}})$ distribution is used to construct three templates [4]. The first one is for the electrons reconstructed with correct charge sign, the last two are for the charge confusion positrons and protons. The electron signal template is taken from high purity electron data below 100 GeV and from electron Monte Carlo simulation above 100 GeV. The charge confusion positron background template is from the Monte Carlo simulation. The charge confusion proton template is constructed using charge confusion proton data selected by the ECAL. An illustration of the template fit to the data in the energy range [700–1000] GeV is shown in Figs. S5(a) and S5(b) of the Supplemental Material [21].

In the energy bin [1000–1400] GeV the number of events is determined by fitting the Λ_{ECAL} template. In this energy bin the Λ_{ECAL} distribution for antiprotons and charge confusion protons is found to be the same as for ordinary protons. Therefore, to reduce the statistical fluctuation, the charge confusion proton template is constructed using proton data. This is done by selecting protons with the TRD and the tracker, and also requiring the ratio of the ECAL energy and the tracker rigidity $E/|R| < 1.0$. The Λ_{ECAL} electron template is energy independent for $E >$ 100 GeV [20]; therefore, the electron signal template is constructed using electron data selected by the TRD and the tracker in the energy range [100–1000] GeV to reduce the statistical fluctuation of the template. The shape of the charge confusion positron Λ_{ECAL} template is the same as for the electron signal. The amount of the charge confusion

positron background is estimated from the Monte Carlo simulation by extrapolating the positron flux with Eq. (4) and its fitted parameters in Ref. [4]. It amounts to 3% of the electron signal. An illustration of the template fit to the data in the energy range [1000–1400] GeV is shown in Fig. S6 of the Supplemental Material [21].

In total, 28.1×10^6 electrons are identified in the energy range from 0.5 GeV to 1.4 TeV.

Data analysis.—The isotropic electron flux for the energy bin E_i of width ΔE_i is given by

$$\Phi_{e^-,i} = \frac{N_i}{A_i(1+\delta_i)T_i\Delta E_i}, \quad (1)$$

where the energy is defined at the top of the AMS. The same energy binning as in our previous publications [1,4] is used. N_i is the number of e^- in bin i corrected for the small bin-to-bin migration using the unfolding procedure described in Ref. [27]. A_i is the corresponding effective acceptance that includes geometric acceptance, and the trigger and selection efficiencies. It is calculated from Monte Carlo simulation. T_i is the data collection time.

The small corrections δ_i are estimated by comparing the efficiencies in data and Monte Carlo simulation of every selection cut using information from the detectors unrelated to that cut. The corrections δ_i are found to have a very small energy dependence: from -5% at 1 GeV, decreasing to -2.4% at 10 GeV, and becoming constant at -2.8% above 50 GeV.

The detailed study of the systematic errors is the key part of the analysis. Five sources of systematic uncertainties are identified.

The first source is related to the uncertainty in the template definitions, which includes two parts: the event selection and the statistical fluctuations. To examine the systematic errors associated with the selection, the selection cuts are varied such that the number of events in the corresponding template vary up to 30%. Each variation yields redefined templates. The variation of the number of electrons from the fits with the redefined templates is used to estimate the associated systematic error. This error amounts to $<0.3\%$ of the flux for the entire energy range. The systematic error associated with fluctuations is measured by varying the shape of the templates within the statistical uncertainties. This error amounts to $<0.4\%$ of the flux below 500 GeV, $\leq 2\%$ below 1000 GeV, and 3.5% in the last energy bin [1000–1400] GeV. These two errors are added in quadrature.

The second source is the uncertainty in the magnitude of the charge confusion. The amount of charge confusion is well reproduced by the Monte Carlo simulation (see Ref. [4], Fig. S1). The corresponding systematic error accounts for the small differences between data and the Monte Carlo simulation. The charge confusion error is $\leq 0.6\%$ of the flux below 500 GeV, $\leq 2\%$ in the range [500–1000] GeV, and 3% in the last bin [1000–1400] GeV.

The third source is the uncertainty in the efficiency corrections δ_i. The corresponding error amounts to 4% of the flux at 0.5 GeV, it decreases to 1.1% at 3 GeV, and slowly rises to 2.5% at [1000–1400] GeV. This includes a correlated systematic error on the flux normalization, which is estimated to be 1% of the flux independent of energy. This 1% error is subtracted in quadrature from the total systematic error for all the fits in this Letter.

The fourth source is the uncertainty in the magnitude of the event bin-to-bin migration due to the finite energy resolution. The bin widths ΔE_i are chosen to be at least 2 times the energy resolution to minimize migration effects [1,3]. Unfolding the measured fluxes shows that the bin-to-bin migration is small: the corresponding error is 2% of the flux at 0.5 GeV and it decreases to $<0.2\%$ above 10 GeV.

The fifth source is the uncertainty in the energy scale, which causes simultaneous shifts in the energy measurement of both electrons and positrons. As discussed in detail in Ref. [20], typical energy scale errors are 4% at 0.5 GeV, 2% from 2 to 300 GeV, and 2.6% at 1.4 TeV.

The total systematic error of the electron flux is taken as the quadratic sum of the four sources: definition of templates, charge confusion, the efficiency corrections, and bin-to-bin migration. The energy scale error is treated as an uncertainty of the bin boundaries.

Several independent analyses were performed on the same data sample by different study groups [11]. The results of those analyses are consistent with the results presented in this Letter.

Results.—The measured electron flux including statistical and systematic errors is presented in Table SI of the Supplemental Material [21] as a function of the energy at the top of AMS. The table includes spectrally weighted mean energy $\tilde{E}$ calculated following Ref. [28] for a flux $\propto E^{-3}$ and the energy scale uncertainty on $\tilde{E}$. Results presented in Table SI are consistent with and supersede our earlier results [1], which were based on 1/3 of the current statistics and cover only 1/2 of the current energy range.

The positron fraction, $\Phi_{e^+}/(\Phi_{e^+}+\Phi_{e^-})$, and the combined (electron + positron) flux, $(\Phi_{e^+}+\Phi_{e^-})$, both based on the electron flux of this Letter and our most recent positron flux [4] are also provided in Table SII of the Supplemental Material [21] with the systematic errors calculated from the systematic uncertainties of positron and electron fluxes that account for correlations due to the calculation of the acceptance.

Figure 1 shows the AMS results on the electron spectrum (i.e., the flux scaled with $\tilde{E}^3$, $\tilde{E}^3\Phi_{e^-}$) in comparison with the most recent AMS positron spectrum [4] scaled by a factor of 10. As seen, the electron and positron spectra have distinctly different magnitudes and energy dependences. Several checks were performed on the same negative rigidity data sample by tightening the selection criteria yielding consistent results. One of these checks with tighter ECAL cut is shown in Fig. S7 of the Supplemental Material [21].

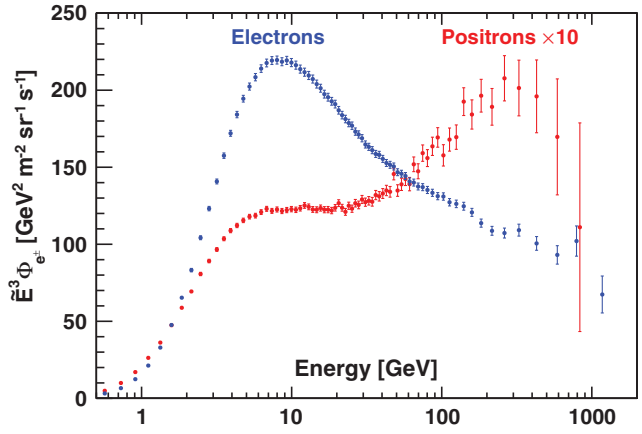

FIG. 1. The AMS electron (blue data points) and positron (red data points, multiplied by 10) spectra ($\tilde{E}^3\Phi_{e^\pm}$). For display purposes the electron data point at ~830 GeV is slightly shifted horizontally to avoid overlap with the positron point. As seen, the electron spectrum has distinctly different magnitude and energy dependence compared to that of positrons.

The AMS results on the electron spectrum together with earlier measurements [24,29–34] are shown in Fig. 2(a). The AMS results significantly improve the precision and extend the measurements to the uncharted high energy region. The positron fraction results together with earlier measurements [24,29–34] are presented in Fig. 2(b). The sum of the electron and positron [4] spectra is compared to the recent measurements of the combined electron and positron spectrum [35–39] in Fig. 2(c).

To examine the energy dependence of the electron flux in a model-independent way, the flux spectral index γ is calculated from

$$\gamma = d[\log(\Phi)]/d[\log(E)], \tag{2}$$

over nonoverlapping energy intervals which are chosen to have sufficient sensitivity to the spectral index. The energy interval boundaries are 3.36, 5.00, 7.10, 10.32, 17.98, 27.25, 55.58, 90.19, 148.81, 370, and 1400 GeV. The results are presented in Fig. 3(a) together with the positron results [4]. They are stable against the variation of energy range boundaries as verified by shifting the boundaries to higher and lower values by one or two energy bins (see Fig. S8 of the Supplemental Material [21]). As seen in Fig. 3(a), both the electron and positron indices decrease (soften) rapidly with energy below ~10 GeV, and then they both start increasing (harden) at > 20 GeV. In particular, the electron spectral index increases from $\gamma = -3.295 \pm 0.026$ in the energy range [17.98–27.25] GeV to an average $\gamma = -3.180 \pm 0.008$ in the range [55.58–1400] GeV, where it is nearly energy independent. As seen in Fig. 3(a), the behavior of the electron and positron spectral indices is distinctly different.

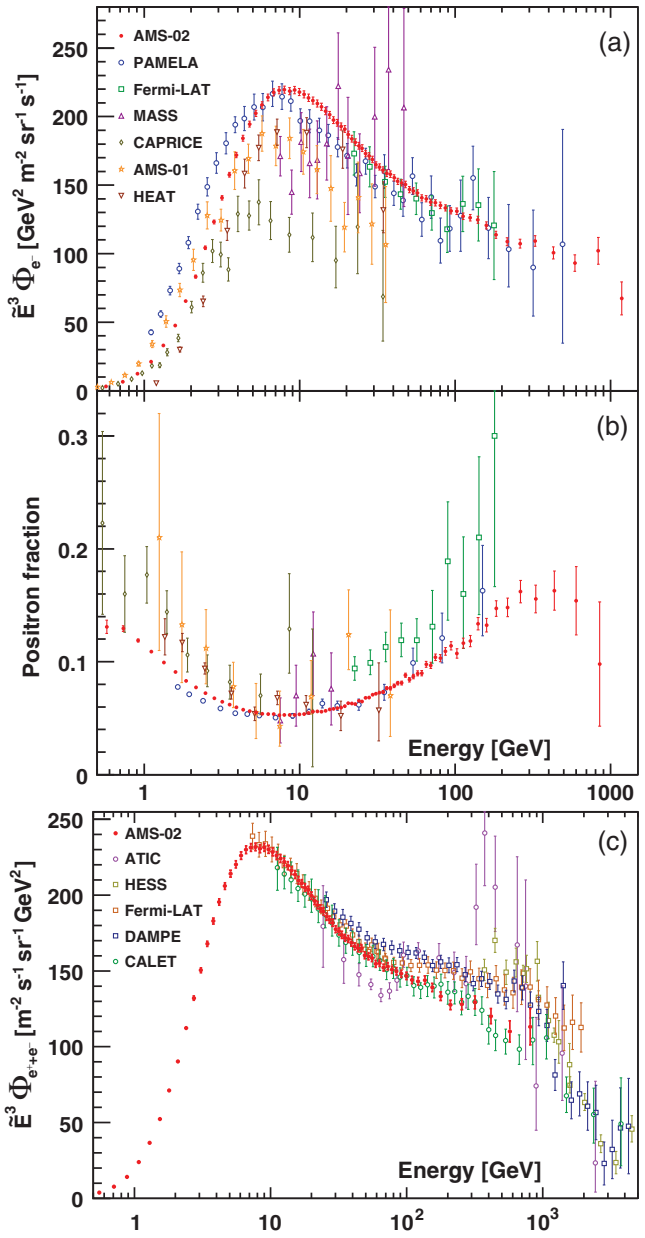

FIG. 2. (a) The AMS electron spectrum ($\tilde{E}^3\Phi_{e^-}$, red data points, placed at $\tilde{E}$) and (b) the AMS positron fraction (red data points, placed at the bin center). Also shown are earlier measurements from PAMELA [29], Fermi-LAT [30], MASS [31], CAPRICE [32], AMS-01 [24,33], and HEAT [34]. (c) The sum of AMS electron and positron [4] spectra (red data points, placed at $\tilde{E}$). Also shown are recent measurements of the combined $(e^+ + e^-)$ flux from ATIC [35], HESS [36], Fermi-LAT [37], DAMPE [38], and CALET [39].

To determine the transition energy E_0 where the change of the electron spectral index occurs, we use a double power law approximation:

$$\Phi_{e^-}(E) = \begin{cases} C(E/20.04\ \text{GeV})^{\gamma} & E \le E_0 \\ C(E/20.04\ \text{GeV})^{\gamma} & (E/E_0)^{\Delta\gamma} E > E_0. \end{cases} \tag{3}$$

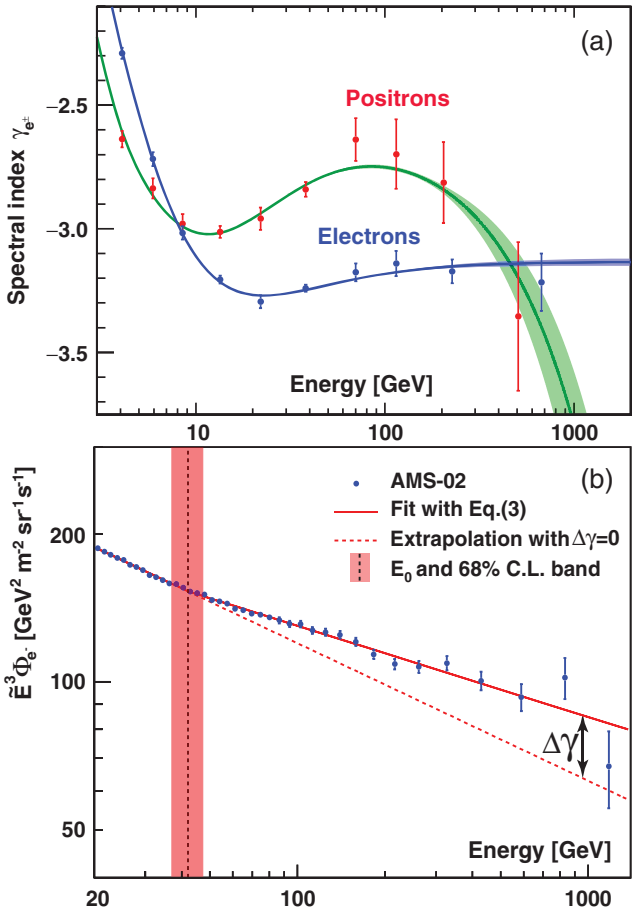

FIG. 3. (a) The spectral indices of the AMS electron (blue data points) and positron [4] (red data points) fluxes in nonoverlapping energy intervals. They show distinctly different behavior. The blue band represents the 68% C.L. interval of the fit of Eq. (5) to the electron flux (see text). The green band represents the 68% C.L. interval of a fit to the positron flux [Eq. (4) in Ref. [4]]. (b) A double power law fit of Eq. (3) to the electron flux in the energy range [20.04–1400] GeV. The blue data points are the measured electron flux values scaled by $\tilde{E}^3$. The fitted function is represented by the solid red line. The vertical dashed line and the red band correspond to the value and the error of the energy E_0 where the change of the spectral index occurs and $\Delta\gamma = 0.094 \pm 0.014$ is the magnitude of the spectral index change; see Eq. (3). The dashed red line is the extrapolation of the power law below E_0 into the higher energy region [or $\Delta\gamma = 0$ in Eq. (3)].

A fit to the data is performed in the energy range [20.04–1400] GeV. The energy range boundary of 20.04 GeV is chosen to be above the observed range of time dependence based on the analysis of Ref. [2]. The results are presented in Fig. 3(b). The fit yields $E_0 = 42.1^{+5.4}_{-5.2}$ GeV for the energy where the spectral index increases with $C = 2.335^{+0.014}_{-0.019} \times 10^{-2}$ [m^2 sr s GeV]$^{-1}$, $\gamma = -3.280^{+0.014}_{-0.016}$, $\Delta\gamma = 0.094 \pm 0.014$, and $\chi^2/\text{d.o.f.} = 17.9/36$. The energy E_0 corresponds to the beginning of a significant excess of the electron flux (i.e., spectral hardening at E_0) compared to the lower energy trends. The spectral index change by $\Delta\gamma$ is clearly visible in Fig. 3(b). Note that the choice of the value 20.04 GeV in Eq. (3) affects only the normalization C. It does not affect the fitted values of E_0, γ, and $\Delta\gamma$.

To investigate the existence of a finite energy cutoff as seen in the positron flux [4], the electron flux is fitted starting from the lower boundary of the E_0 bin [41.61–44.00] GeV with

$$\Phi_{e^-}(E) = C_s(E/41.61\ \text{GeV})^{\gamma_s}\exp(-E/E_s). \quad (4)$$

A fit to data in the energy range [41.61–1400] GeV, described in the Supplemental Material [21], yields the inverse cutoff energy $1/E_s = 0.00^{+0.08}_{-0.00}$ TeV^{-1} with $\chi^2/\text{d.o.f.} = 15.2/23$. A study of the cutoff significance shows that $E_s < 1.9$ TeV is excluded at the 5σ level. These results are presented in Fig. S9 of the Supplemental Material [21].

New sources of high energy positrons, such as dark matter, may also produce an equal amount of high energy electrons [5,7]. We test this hypothesis using the source term from our recent Letter on positrons [4]. This analysis shows that our electron flux data are consistent both with the existence of a high energy electron source term identical to that of positrons and also with the absence of such a term (see the description of the analysis and Fig. S10 in the Supplemental Material [22]). Thus it is not possible to extract any additional information on the existence and properties of the source term using the electron flux alone.

In addition to a small contribution of secondary electrons produced in the collisions of ordinary cosmic rays with the interstellar gas [40], there are several astrophysical sources of primary cosmic-ray electrons. It is assumed that there are only a few astrophysical sources of high energy electrons in the vicinity of the Solar System each making a power-law-like contribution to the electron flux [41,42]. In addition, there are several physics effects which may introduce some spectral features in the original fluxes [43,44]. Therefore, it is important to know the minimal number of distinct power law functions needed to accurately describe the AMS electron flux.

We found that in the entire energy range [0.5–1400] GeV the electron flux is well described by the sum of two power law components:

$$\Phi_{e^-}(E) = \frac{E^2}{\hat{E}^2}[1+(\hat{E}/E_t)^{\Delta\gamma_t}]^{-1}[C_a(\hat{E}/E_a)^{\gamma_a} + C_b(\hat{E}/E_b)^{\gamma_b}]. \quad (5)$$

In order to account for the effects related to the complex spectral behavior of the electron flux at energies below ~10 GeV [2,43], an additional transition term, $[1+(\hat{E}/E_t)^{\Delta\gamma_t}]^{-1}$, is introduced. It is characterized by a transition energy E_t and a spectral index $\Delta\gamma_t$. It has vanishing impact on the flux behavior at energies above

E_t (e.g., <0.7% above 40 GeV) and its effect is similar to the transition described by the dashed line in Fig. SM 3 of Ref. [2]. The two components, a and b, correspond to two power law functions with corresponding normalization factors C_a and C_b, and spectral indices γ_a and γ_b. To account for solar modulation effects, the force-field approximation [45] is used, with the energy of particles in the interstellar space $\hat{E} = E + \varphi_{e^-}$ and the effective modulation potential φ_{e^-}. The constant E_a is chosen to be 20 GeV to minimize the correlation between parameters C_a and γ_a, and the constant E_b is chosen to be 300 GeV to minimize correlation between the parameters C_b and γ_b. A fit to the data in the energy range [0.5–1400] GeV yields $\varphi_{e^-} = 0.87 \pm 0.12$ GeV for the effective potential, $E_t = 3.94 \pm 0.21$ GeV and $\Delta\gamma_t = -2.14 \pm 0.09$ for the parameters of the transition term, $C_a = (1.13 \pm 0.08) \times 10^{-2}$ $[\mathrm{m^2\,sr\,s\,GeV}]^{-1}$ and $\gamma_a = -4.31 \pm 0.13$ for the power law a, and $C_b = (3.96 \pm 0.04) \times 10^{-6}$ $[\mathrm{m^2\,sr\,s\,GeV}]^{-1}$ and $\gamma_b = -3.14 \pm 0.02$ for the power law b, with $\chi^2/\mathrm{d.o.f.} = 36.5/68$. The result of the fit is presented in Fig. 4. The energy dependence of the electron spectral index corresponding to the results of the fit of Eq. (5) is shown in Fig. 3(a) as a blue 68% C.L. band. Studies of the time dependence of the fit parameters show that the only time-dependent parameter is φ_{e^-} and the other parameters do not show significant time variations (see description of the analysis and Fig. S11 in the Supplemental Material [21]). Note that the choice of the E_a and E_b constants does not affect the shapes nor the magnitudes of the terms a and b shown in Fig. 4. We conclude that in the energy range [0.5–1400] GeV the sum of two power law functions with the additional transition term provides an excellent description of the data.

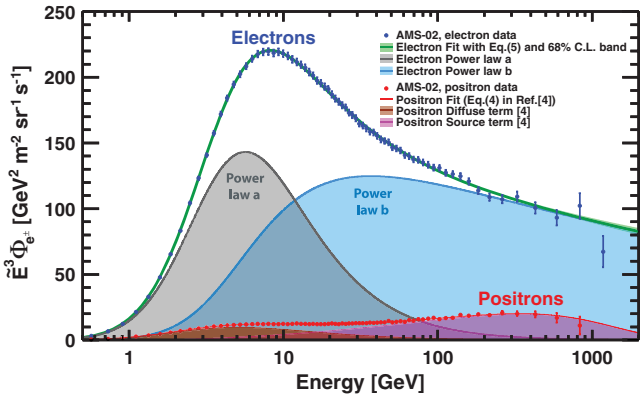

FIG. 4. The two power law fit of Eq. (5) to the electron flux data in the energy range [0.5–1400] GeV with 68% C.L. (green band). The two power law components a and b of Eq. (5) are represented by the gray and blue areas, respectively. Also shown are the positron spectrum together with the fit of Eq. (4) of Ref. [4] including the positron diffuse (i.e., interstellar secondary production) term (the brown area) and positron source term (the magenta area) contributions.

As seen in Fig. 4, these functions are very different in shape and in magnitude from those describing the positron flux [4]. Contrary to the interstellar secondary production term in positrons, which corresponds to positrons produced in collisions of ordinary cosmic rays (protons and helium) with the interstellar gas and dominates the positron flux below 10 GeV, the power law a contribution exceeds the expected secondary electron or positron production by a factor of ~20 (see Ref. [40]). The power law b contribution, which dominates the electron flux at high energies >40 GeV, significantly exceeds the magnitude of the positron source term [4], which has an exponential energy cutoff at 810^{+310}_{-180} GeV (see Fig. 4). The electron flux does not have an energy cutoff below 1.9 TeV at the 5σ level. Therefore, the excess of the electron flux at $E_0 = 42.1^{+5.4}_{-5.2}$ GeV compared to the lower energy trends has a different nature compared to positron flux excess at 25.2 ± 1.8 GeV. This is clear evidence that most cosmic-ray electrons originate from different sources than cosmic-ray positrons.

An analysis of the arrival directions of electrons and positrons was presented in Ref. [3]. A similar analysis was performed using the electron data of this Letter [46]. The electron flux is found to be consistent with isotropy; the upper limit on the amplitude of the dipole anisotropy is $\delta < 0.005$ at the 95% C.L. for energies above 16 GeV.

In conclusion, we have presented the high statistics precision measurements of the electron flux from 0.5 GeV to 1.4 TeV, with detailed study of systematic uncertainties based on a data sample of 28.1×10^6 electrons. In the entire energy range the electron and positron spectra have distinctly different magnitudes and energy dependences. The electron flux exhibits a significant excess starting from $42.1^{+5.4}_{-5.2}$ GeV compared to the lower energy trends, but the nature of this excess is different from the positron flux excess above 25.2 ± 1.8 GeV. Contrary to the positron flux, which has an exponential energy cutoff of 810^{+310}_{-180} GeV, at the 5σ level the electron flux does not have an energy cutoff below 1.9 TeV. In the entire energy range from 0.5 GeV to 1.4 TeV the electron flux is well described by the sum of two power law components. The different behavior of the cosmic-ray electrons and positrons measured by AMS is clear evidence that most high energy electrons originate from different sources than high energy positrons.

We are grateful for important physics discussions with Pasquale Blasi, Fiorenza Donato, Jonathan Ellis, Jonathan Feng, Michael M. Kachelrieß, Mischa Malkov, Igor Moskalenko, Andrii Neronov, Subir Sarkar, and Dmitri Semikoz. We thank former NASA Administrator Daniel S. Goldin for his dedication to the legacy of the ISS as a scientific laboratory and his decision for NASA to fly AMS as a DOE payload. We also acknowledge the

continuous support of the NASA leadership, particularly William H. Gerstenmaier, and of the JSC and MSFC flight control teams that have allowed AMS to operate optimally on the ISS for over seven years. We are grateful for the support of Jim Siegrist and his staff of the DOE including resources from the National Energy Research Scientific Computing Center under Contract No. DE-AC02-05CH11231. We also acknowledge the continuous support from MIT and its School of Science, Michael Sipser, and Boleslaw Wyslouch. Research supported by São Paulo Research Foundation (FAPESP) Grant No. 2014/19149-7, Brazil; CAS, NSFC, MOST, the provincial governments of Shandong, Jiangsu, Guangdong, and the China Scholarship Council, China; CNRS/IN2P3, CNES, Enigmass, and the ANR, France; Pascale Ehrenfreund, DLR under Grant No. 50OO1403 and JARA-HPC under Project No. JARA0052, Germany; INFN and ASI under ASI-INFN Agreements No. 2013-002-R.0 and No. 2014-037-R.0, Italy; the Consejo Nacional de Ciencia y Tecnología and UNAM, Mexico; FCT under Grant No. PTDC/FIS/122567/2010, Portugal; CIEMAT, IAC, CDTI, and SEIDI-MINECO under Grants No. ESP2017-87055-C2-1-P, No. SEV-2015-0548, No. MDM-2015-0509, and No. RyC-2013-14660, Spain; the Swiss National Science Foundation (SNSF), federal and cantonal authorities, Switzerland; Academia Sinica and the Ministry of Science and Technology (MOST) under Grants No. 103-2112-M-006-018-MY3, No. 105-2112-M-001-003, and No. CDA-105-M06, former Presidents of Academia Sinica Yuan-Tseh Lee and Chi-Huey Wong and former Ministers of MOST Maw-Kuen Wu and Luo-Chuan Lee, Taiwan; the Turkish Atomic Energy Authority under Grant No. 2017TAEK(CERN)A5.H6.F2-15, Turkey; and NSF Grants No. 14255202 and No. 1551980, Wyle Laboratories Grant No. 2014/T72497, and NASA NESSF Grant No. HELIO15F-0005, U.S. We gratefully acknowledge the strong support from CERN including Fabiola Gianotti, and the CERN IT department including Bernd Panzer-Steindel, and from the European Space Agency including Johann-Dietrich Wörner and Simonetta Di Pippo.

*Also at: ASI, I–00133 Roma, Italy.
†Also at: ASI Space Science Data Center (SSDC), I–00133 Roma, Italy.
‡Also at: Wuhan University, Wuhan, 430072, China.

[1] M. Aguilar *et al.*, Phys. Rev. Lett. **113**, 121102 (2014); **113**, 221102 (2014).
[2] M. Aguilar *et al.*, Phys. Rev. Lett. **121**, 051102 (2018).
[3] M. Aguilar *et al.*, Phys. Rev. Lett. **110**, 141102 (2013); L. Accardo *et al.*, Phys. Rev. Lett. **113**, 121101 (2014).
[4] M. Aguilar *et al.*, Phys. Rev. Lett. **122**, 041102 (2019).
[5] P. D. Serpico, Astropart. Phys. **39–40**, 2 (2012); T. Linden and S. Profumo, Astrophys. J. **772**, 18 (2013); P. Mertsch and S. Sarkar, Phys. Rev. D **90**, 061301 (2014); M. Di Mauro, F. Donato, N. Fornengo, R. Lineros, and A. Vittino, J. Cosmol. Astropart. Phys. 04 (2014) 006; N. Tomassetti and F. Donato, Astrophys. J. Lett. **803**, L15 (2015); D. Hooper, I. Cholis, T. Linden, and K. Fang, Phys. Rev. D **96**, 103013 (2017); W. Liu, X. J. Bi, S. J. Lin, B. B. Wang, and P. F. Yin, Phys. Rev. D **96**, 023006 (2017); S. Profumo, J. Reynoso-Cordova, N. Kaaz, and M. Silverman, Phys. Rev. D **97**, 123008 (2018).
[6] R. Cowsik, B. Burch, and T. Madziwa-Nussinov, Astrophys. J. **786**, 124 (2014); K. Blum, B. Katz, and E. Waxman, Phys. Rev. Lett. **111**, 211101 (2013).
[7] M. S. Turner and F. Wilczek, Phys. Rev. D **42**, 1001 (1990); J. Ellis, AIP Conf. Proc. **516**, 21 (2000); H. C. Cheng, J. L. Feng, and K. T. Matchev, Phys. Rev. Lett. **89**, 211301 (2002); G. Kane, R. Lu, and S. Watson, Phys. Lett. B **681**, 151 (2009); J. Kopp, Phys. Rev. D **88**, 076013 (2013); C. H. Chen, C. W. Chiang, and T. Nomura, Phys. Lett. B **747**, 495 (2015); H. C. Cheng, W. C. Huang, X. Huang, I. Low, Y. L. Sming Tsia, and Q. Yuan, J. Cosmol. Astropart. Phys. 03 (2017) 041; S. J. Lin, Q. Yuan, and X. J. Bi, Phys. Rev. D **91**, 063508 (2015); Y. Bai, J. Berger, and S. Lu, Phys. Rev. D **97**, 115012 (2018).
[8] L. Ali Cavasonza, H. Gast, M. Krämer, M. Pellen, and S. Schael, Astrophys. J. **839**, 36 (2017).
[9] M. Boschini *et al.*, Astrophys. J. **854**, 94 (2018).
[10] M. Kachelrieß, A. Neronov, and D. V. Semikoz, Phys. Rev. D **97**, 063011 (2018).
[11] M. Aguilar (AMS Collaboration), Properties of cosmic-ray elementary particles (antiprotons, protons, positrons, and electrons) measured by AMS (to be published).
[12] A. Kounine, Int. J. Mod. Phys. E **21**, 1230005 (2012); S. Rosier-Lees, in Proceedings of the 19th Symposium on Astroparticle Physics in the Netherlands, Beekbergen, 2014 (unpublished); S. C. C. Ting, Nucl. Phys. B, Proc. Suppl. **243–244**, 12 (2013); S. C. Lee, in Proceedings of the 20th International Conference on Supersymmetry and Unification of Fundamental Interactions (SUSY 2012), Beijing, 2012 (unpublished); M. Aguilar, in Proceedings of the XL International Meeting on Fundamental Physics, Centro de Ciencias de Benasque Pedro Pascual, 2012 (unpublished); S. Schael, in Proceedings of the 10th Symposium on Sources and Detection of Dark Matter and Dark Energy in the Universe, Los Angeles, 2012 (unpublished); B. Bertucci, Proc. Sci. EPS-HEP2011 (**2011**) 067; M. Incagli, AIP Conf. Proc. **1223**, 43 (2010); R. Battiston, Nucl. Instrum. Methods Phys. Res., Sect. A **588**, 227 (2008).
[13] F. Hauler *et al.*, IEEE Trans. Nucl. Sci. **51**, 1365 (2004); Ph. Doetinchem *et al.*, Nucl. Instrum. Methods Phys. Res., Sect. A **558**, 526 (2006); Th. Kirn, Nucl. Instrum. Methods Phys. Res., Sect. A **706**, 43 (2013).
[14] V. Bindi *et al.*, Nucl. Instrum. Methods Phys. Res., Sect. A **743**, 22 (2014), and references therein.
[15] B. Alpat *et al.*, Nucl. Instrum. Methods Phys. Res., Sect. A **613**, 207 (2010).
[16] K. Lübelsmeyer *et al.*, Nucl. Instrum. Methods Phys. Res., Sect. A **654**, 639 (2011).
[17] C. Adloff *et al.*, Nucl. Instrum. Methods Phys. Res., Sect. A **714**, 147 (2013).

[18] Ph. von Doetinchem, W. Karpinski, Th. Kirn, K. Lübelsmeyer, St. Schael, and M. Wlochal, Nucl. Phys. B, Proc. Suppl. **197**, 15 (2009).

[19] M. Aguilar-Benitez *et al.*, Nucl. Instrum. Methods Phys. Res., Sect. A **614**, 237 (2010); F. Giovacchini, Nucl. Instrum. Methods Phys. Res., Sect. A **766**, 57 (2014).

[20] A. Kounine, Z. Weng, W. Xu, and C. Zhang, Nucl. Instrum. Methods Phys. Res., Sect. A **869**, 110 (2017).

[21] See Supplemental Material at http://link.aps.org/supplemental/10.1103/PhysRevLett.122.101101, for the tabulated e^- flux, the positron fraction, the sum of electron and positron fluxes, and their statistical and systematic errors; for figures related to the data comparison with the Monte Carlo simulation, event selection, complementary data analysis, the stability of the electron spectral index; and for the descriptions and figures related to the energy cutoff, positron source term, and the time dependence of the fit parameters.

[22] J. Allison *et al.*, Nucl. Instrum. Methods Phys. Res., Sect. A **835**, 186 (2016); S. Agostinelli *et al.*, Nucl. Instrum. Methods Phys. Res., Sect. A **506**, 250 (2003).

[23] C. Størmer, *The Polar Aurora* (Oxford University Press, London, 1950).

[24] J. Alcaraz *et al.*, Phys. Lett. B **484**, 10 (2000).

[25] E. Thébault *et al.*, Earth Planets Space **67**, 79 (2015); C. C. Finlay, Geophys. J. Int. **183**, 1216 (2010).

[26] M. Aguilar *et al.*, Phys. Rev. Lett. **117**, 091103 (2016).

[27] M. Aguilar *et al.*, Phys. Rev. Lett. **114**, 171103 (2015).

[28] G. D. Lafferty and T. R. Wyatt, Nucl. Instrum. Methods Phys. Res., Sect. A **355**, 541 (1995). We have used Eq. (6) with $\tilde{E} \equiv x_{lw}$.

[29] O. Adriani *et al.*, Phys. Rev. Lett. **106**, 201101 (2011).

[30] M. Ackermann *et al.*, Phys. Rev. Lett. **108**, 011103 (2012).

[31] C. Grimani *et al.*, Astron. Astrophys. **392**, 287 (2002).

[32] M. Boezio *et al.*, Adv. Space Res. **27**, 669 (2001).

[33] M. Aguilar *et al.*, Phys. Lett. B **646**, 145 (2007).

[34] S. W. Barwick *et al.*, Astrophys. J. **498**, 779 (1998); M. A. DuVernois *et al.*, Astrophys. J. **559**, 296 (2001); J. J. Beatty *et al.*, Phys. Rev. Lett. **93**, 241102 (2004).

[35] J. Chang *et al.*, Nature (London) **456**, 362 (2008).

[36] F. Aharonian *et al.*, Astron. Astrophys. **508**, 561 (2008); F. Aharonian *et al.*, Phys. Rev. Lett. **101**, 261104 (2008).

[37] S. Abdollahi *et al.*, Phys. Rev. D **95**, 082007 (2017).

[38] G. Ambrosi *et al.* (DAMPE Collaboration), Nature (London) **552**, 63 (2017).

[39] O. Adriani *et al.*, Phys. Rev. Lett. **120**, 261102 (2018).

[40] I. V. Moskalenko and A. W. Strong, Astrophys. J. **493**, 694 (1998); A. E. Vladimirov, S. W. Digel, G. Jóhannesson, P. F. Michelson, I. V. Moskalenko, P. L. Nolan, E. Orlando, T. A. Porter, and A. W. Strong, Comput. Phys. Commun. **182**, 1156 (2011).

[41] A. M. Hillas, J. Phys. G **31**, R95 (2005); Y. Z. Fan, B. Zhang, and J. Chang, Int. J. Mod. Phys. D **19**, 2011 (2010).

[42] T. Kobayashi, Y. Komori, K. Yoshida, and J. Nishimura, Astrophys. J. **601**, 340 (2004).

[43] A. W. Strong, E. Orlando, and T. R. Jaffe, Astron. Astrophys. **534**, A54 (2011).

[44] Ł. Stawarz, V. Petrosian, and R. D. Blandford, Astrophys. J. **710**, 236 (2010).

[45] R. A. Caballero-Lopez and H. Moraal, J. Geophys. Res. **109**, A01101 (2004); L. Gleeson and W. Axford, Astrophys. J. **154**, 1011 (1968).

[46] M. A. Velasco, Ph.D. thesis, Universidad Complutense de Madrid, 2018; S. Zeissler, Ph.D. thesis, Karlsruhe Institute of Technology, 2018.